Supporting Information

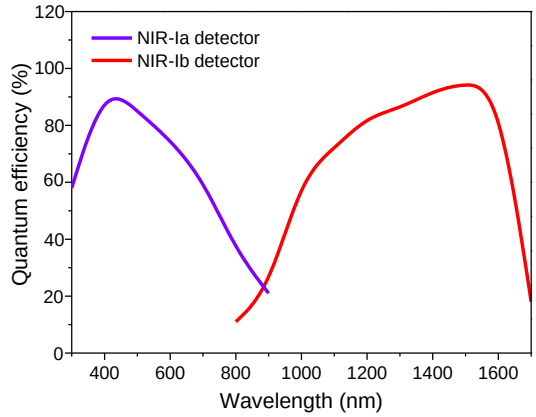

Figure S1. Sensitivity spectrum for NIR-Ia and NIR-Ib window detector

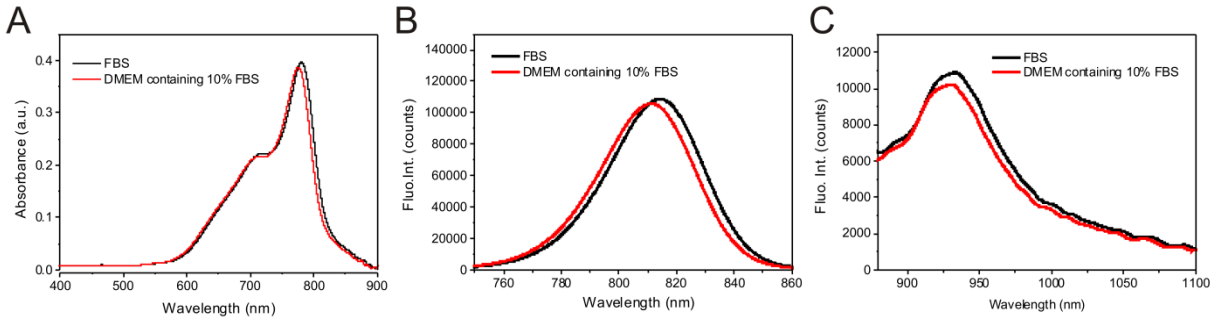

Figure S2: Optical properties of IR-808 in warm serum and cell culture medium. (**A**) UV/Vis absorption spectra of IR-808 in warm serum and cell culture medium, (**B**) NIR-Ia emission spectra of IR-808 in warm serum and cell culture medium (λex = 680 nm) and (**C**) NIR-Ib emission spectra (λex = 808 nm) of IR-808 in warm serum and cell culture medium.

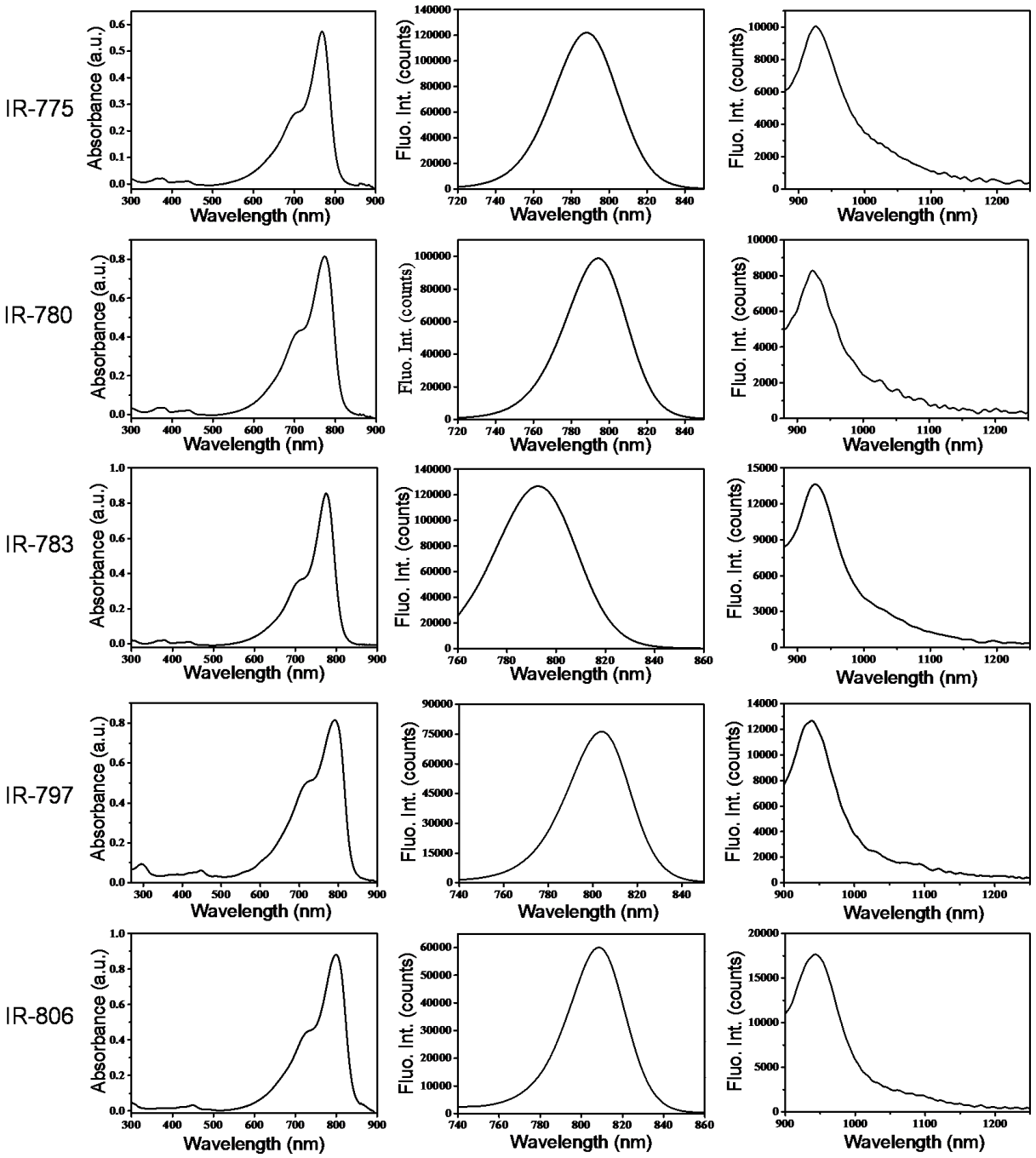

Figure S3: UV–Vis absorption spectra and fluorescence emission spectra of IR-X dyes in water.

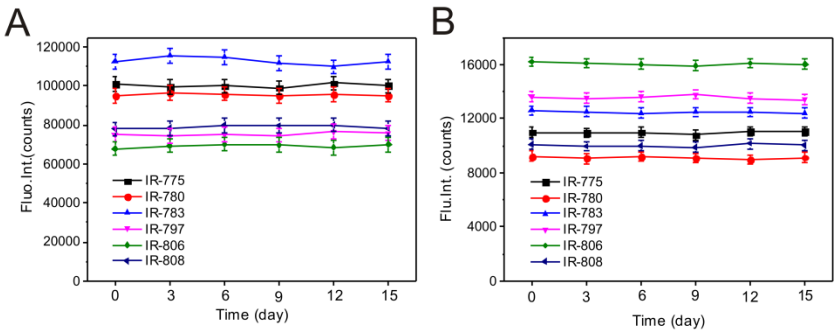

Figure S4. Fluorescent stability of IR-X dyes. (**A**) and (**B**) Fluorescent stability in the NIR-Ia region and NIR-Ib reigon, respectively.

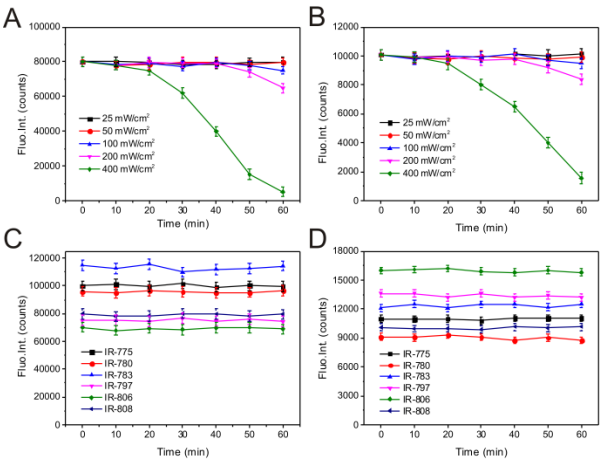

Figure S5. The photostability of IR-X dyes. (**A**) and (**B**) The photostability of IR-808 in NIR-Ia region and NIR-Ib region under 808 nm laser irradiation with different excitation power density, respectively. (**C**) and (**D**) The photostability of IR-X dyes in NIR-Ia region and NIR-Ib region under 808 nm laser irradiation with power density of 50 mW/cm^2.

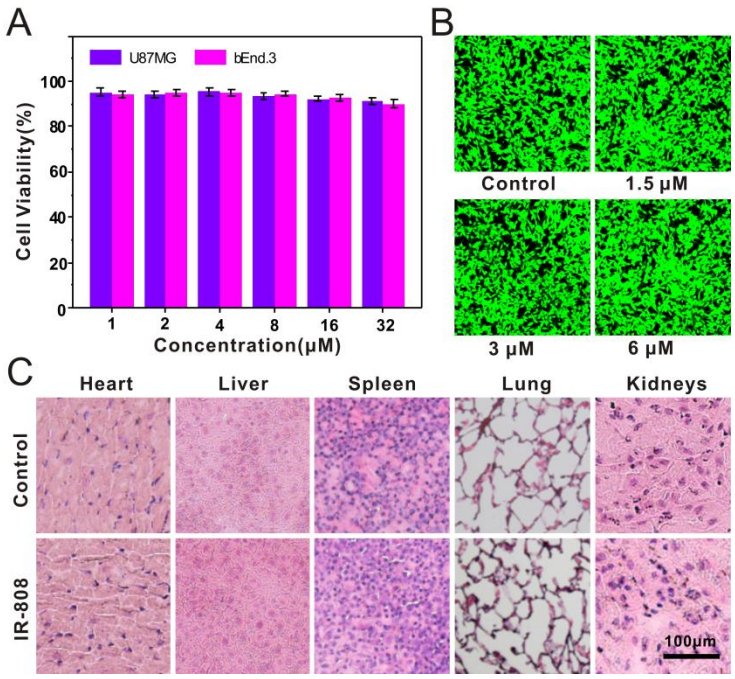

Figure S6: Toxicity analysis of IR-808 dye. (**A**) Viability of U87MG cells (tumour cells) and bEnd.3 (normal cells) incubated with different concentrations of IR-808 for 24 h. (**B**) Fluorescence images of U87 cells incubated with different concentration of IR-808 for 12 h. Viable cells were stained green with calcein-AM, and dead cells were stained red with PI. (**C**) Haematoxylin- and eosin-stained images of major organs excised from mice sacrificed at 72 h post-injection.

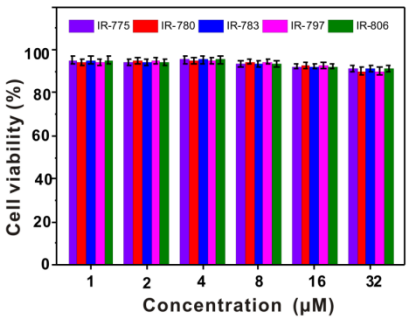

Figure S7. Viability of U87MG cells incubated with different concentrations of IR-X dyes for 24 h.

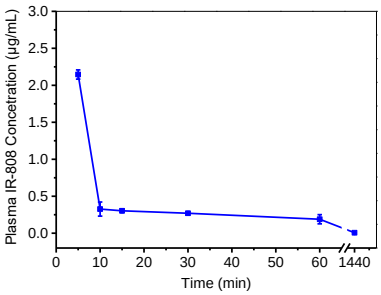

Figure S8. The pharmacokinetic parameter of IR-808 dye after intravenous injection.

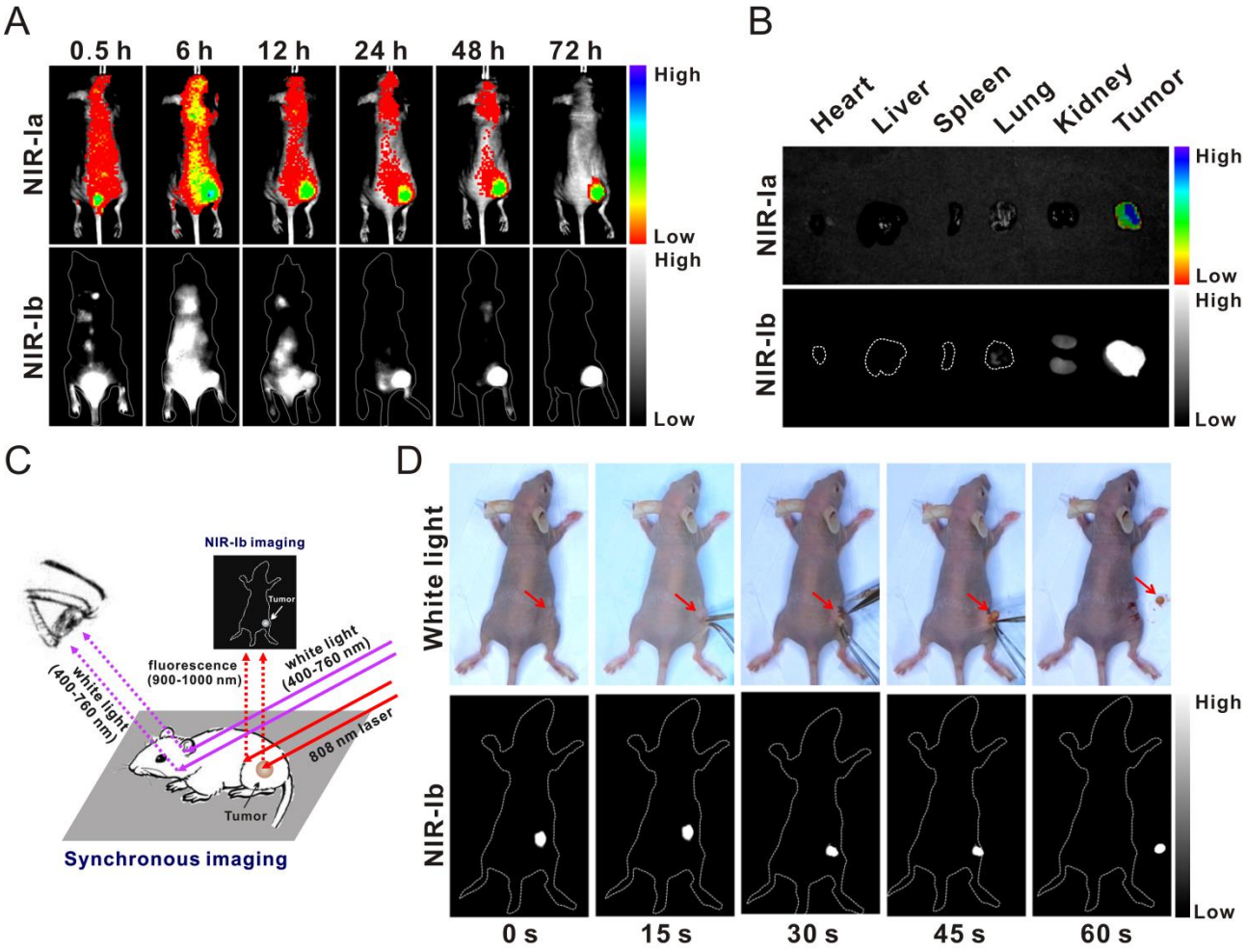

Figure S9: Subcutaneous tumour imaging and image-guided cancer surgery using IR-808 dye. (**A**) *In vivo* NIR-Ia and NIR-Ib images of tumour-bearing mice taken at different time points post-injection. (**B**) *Ex vivo* NIR-Ia and NIR-Ib images of dissected tumours and major organs excised at 72 h post-injection. (**C**) Schematics of image-guided cancer surgery. (**D**) Time-lapse white-light and NIR-Ib images of subcutaneous tumour with respect to the mouse body.

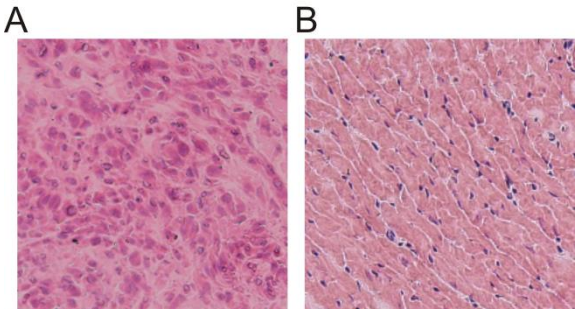

Figure S10. H&E stained histological images. (**A**) H&E stained histological images of tumor bed which had NIR-Ib fluorescence positive foci. (**B**) H&E stained histological images of tumor bed which had no residual NIR-Ib fluorescence positive foci.

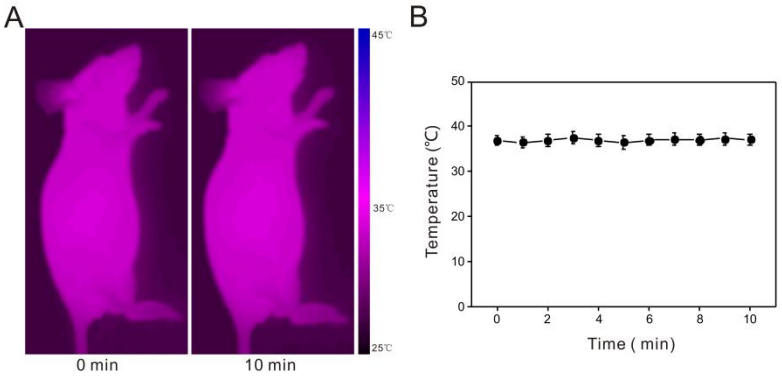

Figure S11. Thermal effect of IR-808 dye emission in NIR-Ib window on the muscle tissue under 808nm excitation (45 mW/cm^2) using an infrared thermal imaging camera (Ti27, Fluke, USA). (**A**) Representative thermal images of mice. (**B**) Thermal effect for tissue during 10 min irradiation of laser.

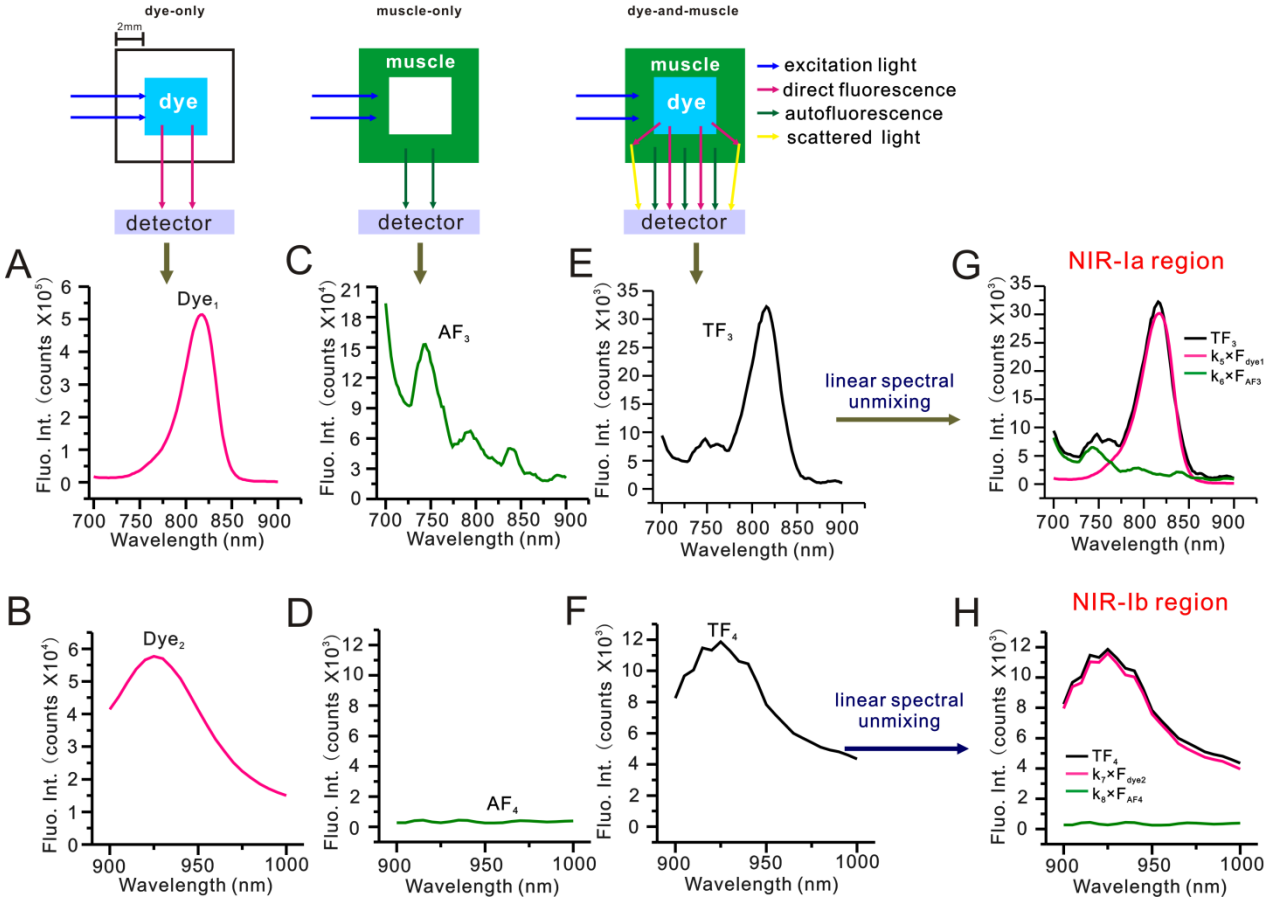

Figure S12: Simulated muscle experiment for evaluating the impact of autofluorescence. (**A**) NIR-Ia and (**B**) NIR-Ib fluorescence spectra of 50 μg/mL IR-808 solution. (**C**) NIR-Ia and (**D**) NIR-Ib autofluorescence spectra of 5% mouse tissue homogenate. (**E**) NIR-Ia and (**F**) NIR-Ib fluorescence spectra of the simulated muscle prior to linear spectral unmixing. (**G**) NIR-Ia and (**H**) NIR-Ib fluorescence spectra of the simulated muscle after linear spectral unmixing. Dye fluorescence and autofluorescence components are highlighted in pink and green, respectively.

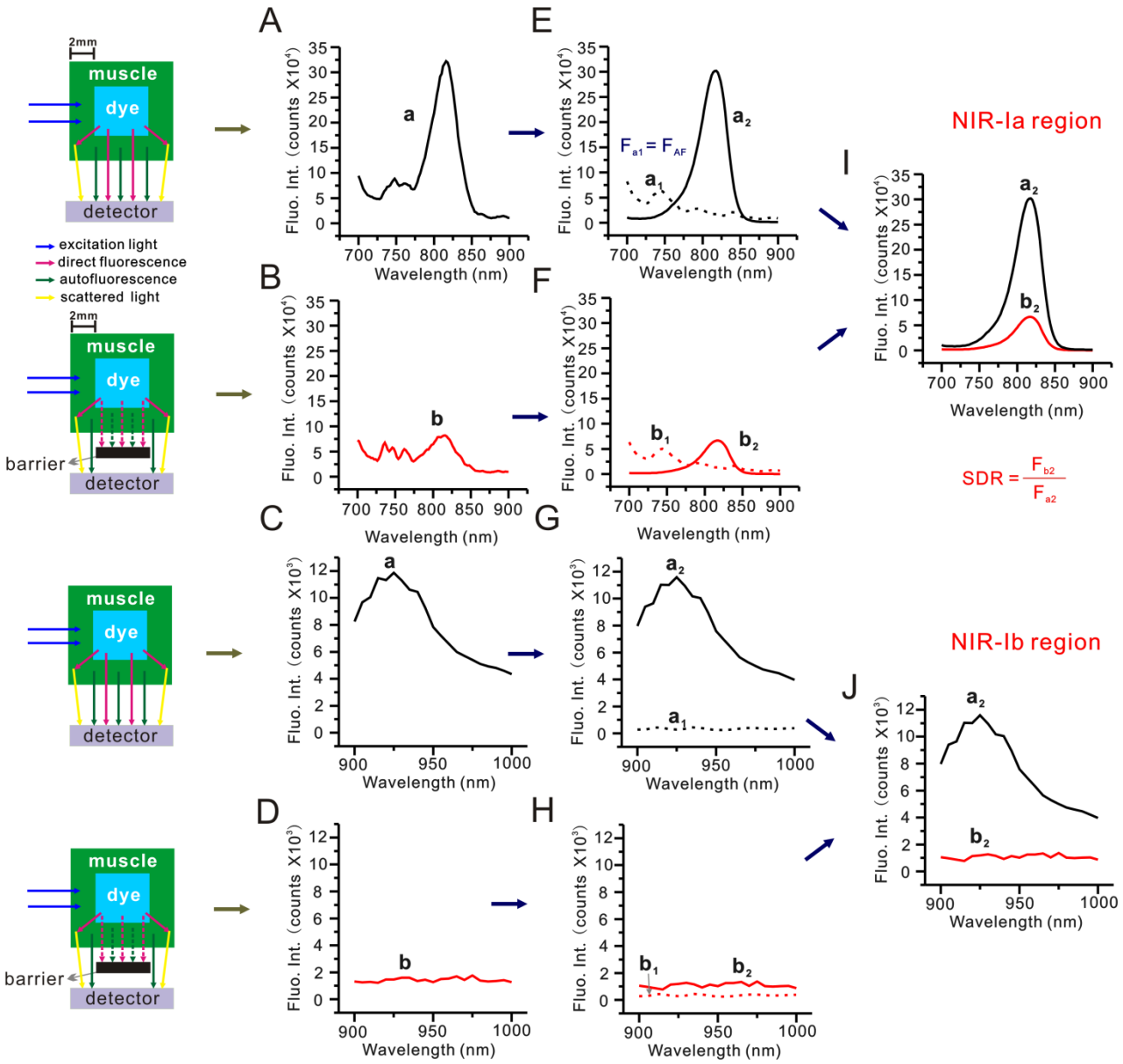

Figure S13: Simulated muscle experiment for evaluating the impact of scattering. (**A**) Unscreened and (**B**) screened NIR-Ia fluorescence spectra of the simulated muscle. (**C**) Unscreened and (**D**) screened NIR-Ib fluorescence spectra of the simulated muscle. (**E**) Unscreened and (**F**) screened NIR-Ia fluorescence spectra after autofluorescence subtraction. (**G**) Unscreened and (**H**) screened NIR-Ib fluorescence spectra after autofluorescence subtraction. (**I**) Schematic diagram for calculating SDR of NIR-Ia and (**J**) NIR-Ib fluorescence imaging.

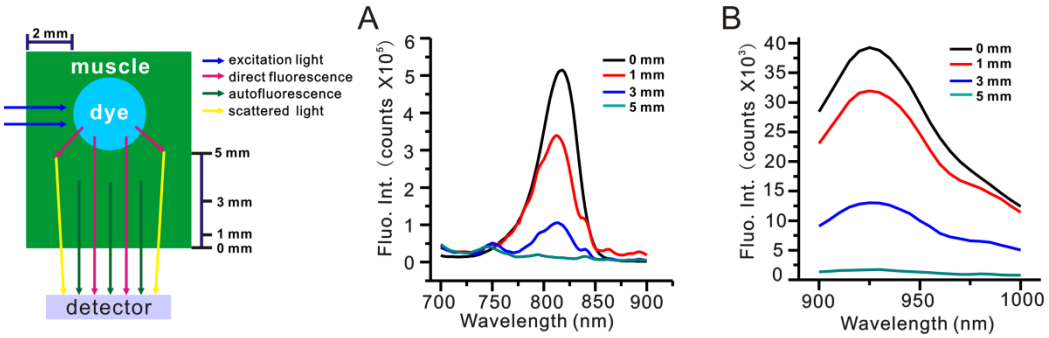

Figure S14: Depth penetration experiment for evaluating the impact of light absorption by biological tissues. (**A**) NIR-Ia and (**B**) NIR-Ib fluorescence spectra of the dye-filled capillary tube at varying depths inside a mouse tissue homogenate-filled cuvette.

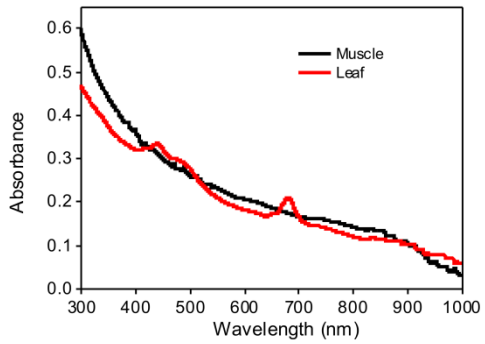

Figure S15. Absorption spectra of 5 % muscle tissues (black) and 5 % leaf tissues (red).

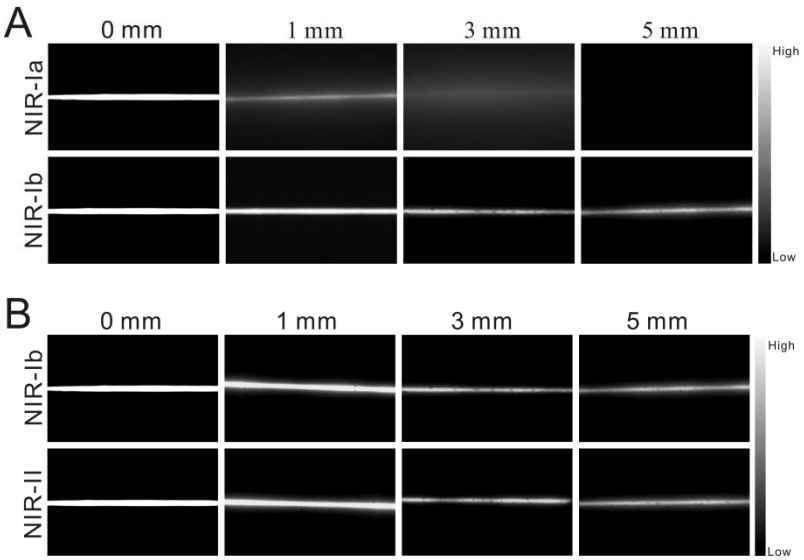

Figure S16. Tissue depth penetration study. (**A**) Fluorescence images of capillaries of IR-808 dye in the NIR-Ia and NIR-Ib region at depths of 0, 1, 3 and 5 mm with 1% intralipid excited at 680 nm and 808 nm, respectively. (**B**) Fluorescence images of capillaries in the NIR-Ib imaging and NIR-II imaging at depths of 0, 1, 3 and 5 mm with 1% intralipid excited at 808 nm.

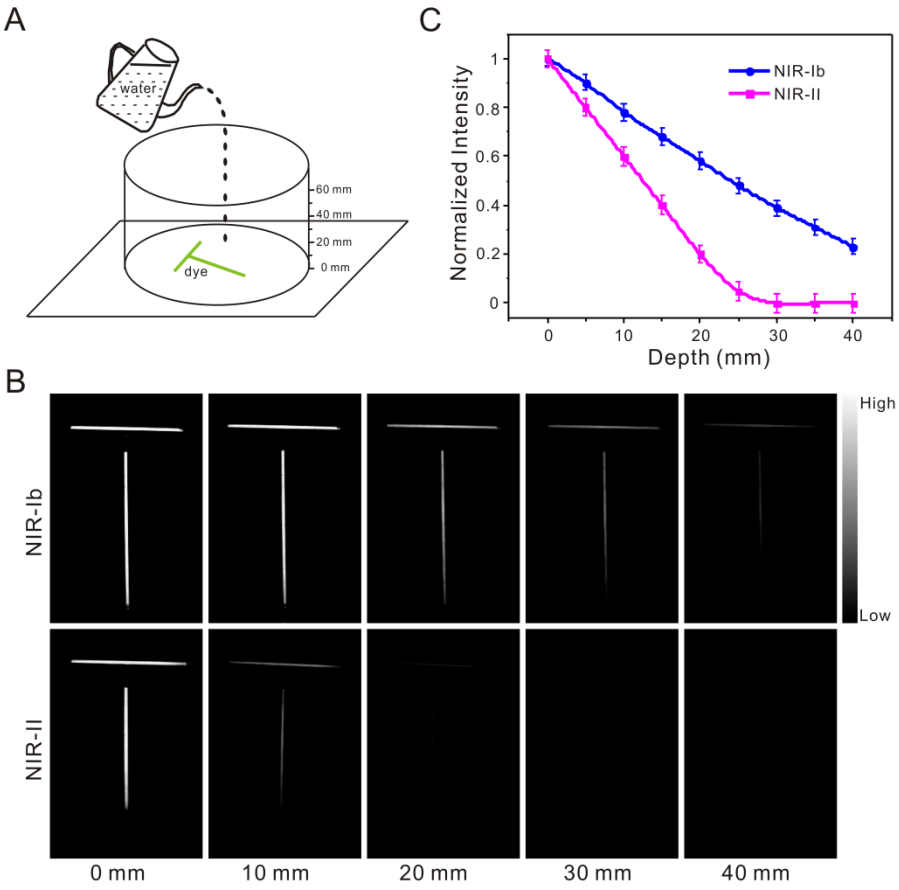

Figure S17. Simulated capillary network experiment for assessing the penetration depth in NIR-Ib and NIR-II fluorescence imaging.(**A**) Schematics of simulated capillary network experiment. (**B**) NIR-Ib and NIR-II images of T-shaped capillary network taken at different water depth. (**C**) Intensity decay at different depth in water.

Table S1. Optical properties of heptamethine dyes in water.

	R group	W	n	λ_{abs} (nm)	λ_{em1} (nm)	λ_{em2} (nm)
IR-775	$-CH_3$	I^-	3	768	790	925
IR-780	$-(CH_2)_2CH_3$	I^-	3	774	795	925
IR-783	$-(CH_2)_4\ SO_3^-$	Na^+	3	776	795	930
IR-797	$-CH_3$	I^-	2	792	805	940
IR-806	$-(CH_2)_4SO_3^-$	Na^+	2	800	810	945
IR-808	$-(CH_2)_5COOH$	I^-	3	776	790	930

Here, R is the position of the substituent group, λ_{abs} is the maximal absorption wavelength of UV/Vis absorption spectra in water, and λ_{em} is the peak wavelength of fluorescence emission spectra in water.

Table S2. Fluorescence quantum yield of IR-X in aqueous solution in the NIR-Ib window

IR-X dyes	IR-775	IR-780	IR-783	IR-797	IR-806	IR-808
Quantum yield (%)in aqueous solution	5.2%	5.5%	6.3%	5.8%	6.1%	5.9%
Quantum yield (%) in DMEM medium	5.3%	5.7%	6.2%	5.9%	6.0%	5.8%

Table S3. ATR of NIR-Ia and NIR-Ib spectra in simulated leaf/muscle experiment

	NIR-Ia	NIR-Ib
Leaf	72.22%	2.87%
Muscle	28.68%	4.29%

Table S4. Fluorescence decay of IR-808 as a function of depth in leaf/mouse tissue homogenate and water.

	NIR-Ia			NIR-Ib		
Depth	Leaf	Muscle	H_2O	Leaf	Muscle	H_2O
0 mm	0.00%	0.00%	0.00%	0.00%	0.00%	0.00%
1 mm	30.17%	37.67%	19.13%	29.34%	18.70%	9.36%
3 mm	72.17%	80.74%	35.64%	61.88%	66.81%	21.11%
5 mm	91.77%	97.72%	52.87%	86.50%	95.69%	33.35%

Table S5. SDR, SBR and SBR_{max} of leaf/mouse tissue homogenate in NIR-Ia and NIR-Ib fluorescence imaging.

			NIR-Ia			NIR-Ib		
			SDR	SBR	$SBR_{max}= (1 – SDR)/SDR$	SDR	SBR	$SBR_{max}= (1 – SDR)/SDR$
Leaf	depth	1 mm	0.25	1.49	3	0.1019	8.01	8.8
		3 mm	0.25	1.29	3	0.1019	7.44	8.8
		5 mm	0.25	1.13	3	0.1019	5.93	8.8
	25 µg/mL		0.25	1.00	3	0.1019	5.58	8.8
	50 µg/mL		0.25	1.00	3	0.1019	5.70	8.8
	100 µg/mL		0.25	1.00	3	0.1019	5.86	8.8
	500 µg/mL		0.25	1.00	3	0.1019	6.02	8.8
Muscle	depth	1 mm	0.2207	2.54	3.5	0.1027	7.73	8.7
		3 mm	0.2207	1.70	3.5	0.1027	6.64	8.7
		5 mm	0.2207	1.23	3.5	0.1027	2.65	8.7